RAA 2016 Vol. **16** No. **2**, 25 (12pp) doi: 10.1088/1674–4527/16/2/025
http://www.raa-journal.org *http://iopscience.iop.org/raa*

***R**esearch in*
***A**stronomy and*
***A**strophysics*

Dense molecular gas tracers in high mass star formation regions

Hong-Jun Ma[1], Yu Gao[1] and Jing-Wen Wu[2,3]

[1] Purple Mountain Observatory/Key Laboratory of Radio Astronomy, Chinese Academy of Sciences, Nanjing 210008, China; *hjma@pmo.ac.cn*, *yugao@pmo.ac.cn*
[2] Department of Physics and Astronomy, University of California, Los Angeles, CA 90095, USA
[3] National Astronomical Observatories, Chinese Academy of Sciences, Beijing 100012, China

Received 2015 April 2; accepted 2015 August 12

Abstract We report the FCRAO observations that mapped HCN (1–0), CS (2–1), HNC (1–0) and HCO^+ (1–0) in ten high-mass star forming cores associated with water masers. We present velocity integrated intensity maps of the four lines for these dense cores, compare their line profiles, and derive physical properties of these cores. We find that these four tracers identify areas with similar properties in these massive dense cores, and in most cases, the emissions of HCN and HCO^+ are stronger than those of HNC and CS. We also use the line ratios of HCO^+/HCN, HNC/HCN and HNC/HCO^+ as the diagnostics to explore the environment of these high-mass star forming regions, and find that most of the cores agree with the model that photodominated regions dominate the radiation field, except for W44, for which the radiation field is similar to an X-ray dominated region.

Key words: ISM: clouds — ISM: molecules — stars: formation

1 INTRODUCTION

Massive stars make significant contributions to their host galaxies' energy budget. The study of the interstellar medium (ISM) helps to understand the mechanism of massive star formation and its feedback to the parent giant molecular clouds (GMCs, Larson 1994). Compared to the surrounding quiescent GMCs, the dense molecular cores normally have higher temperatures and densities, and stars form therein (Beuther & Steinacker 2007). The complex kinetic energy from stellar winds, outflows, HII regions, and supernovae also changes the initial physical conditions of the active star forming regions (Elmegreen & Clemens 1985; Carpenter et al. 2000; Lada & Lada 2003; Reiter et al. 2011b).

Molecular line surveys, among many observational techniques, play one of the most pivotal roles in understanding the physical and chemical evolution of star forming dense cores in GMCs (Evans 1999). In galaxies, single dish and aperture synthesis studies of ^{12}CO and ^{13}CO have shown that the ^{12}CO/^{13}CO line intensity ratios for (1–0) and (2–1) transitions are efficient diagnostic tools to study large scale ISM properties.

Low rotational transitions of CO however cannot well trace dense star forming gas since they are optically thick, and CO has a low dipole moment, thus they probe only a low critical density (^{12}CO and ^{13}CO with $n_{\rm crit} \sim 10^2 - 10^3$ cm^{-3}). Transitions of high dipole moment molecules, such as HCN (1–0), HNC (1–0), CS (2–1) and HCO^+ (1–0), are more common tracers of dense molecular gas ($n_{\rm crit} \sim 10^4 - 10^5$ cm^{-3}, Gao & Solomon 2004a,b), which are better tools to reveal the relationship between molecular gas and star formation (e.g., Shirley et al. 2003; Li et al. 2012). Moreover, the line strengths of HCN, HNC, HCO^+ and CS are affected by environmental properties such as density, temperature and the type and strength of the prevailing radiation field. The line ratios between multiple species are useful for diagnosing some physical conditions, which can be applied to study the characteristics of the sources.

There have been several surveys of massive star formation regions and many detailed studies of individual massive regions using tracers of dense gas (e.g. Plume et al. 1992, 1997; Wu et al. 2005, 2010; Reiter et al. 2011a). This work will focus on a sample of ten massive star forming regions that are in an early phase of star formation, identified by the associated water maser emission (Cesaroni et al. 1988), with multiple molecular dense gas tracers. The parent sample has been well studied by multiple CS line surveys (Plume et al. 1992, 1997), a subsample of which has also been mapped in CS (5–4) and CS (7–6) (Shirley et al. 2003; Wu et al. 2010).

The Milky Way, as our nearest example, has obvious advantages in studying star formation compared to studying other galaxies. The key physical processes that determine how molecular clouds contract and fragment into clumps, cores, individual stars and star clusters can only be probed in the Galaxy. Much of the progress in this subject comes from in-depth case studies of individual star forming regions. However, observations toward Galactic targets have problems with distance determination and selection effects; only with the aid of models can we "look in from the outside" to study properties of the Milky Way. For extragalactic studies, observations are always limited by the current sensitivity and resolution of telescopes, so one can only obtain integrated information over entire star forming regions or, often, over entire galaxies (Gao & Solomon 2004a,b, Garcia-Burillo et al. 2011). Even though it is hard to obtain resolved spatial information of GMCs in nearby galaxies. Some works have been done to link the GMC-scale models to the kpc-scale observations of galaxies (e.g., Wu et al. 2005; Zhang et al. 2014). Leroy et al. (2013) used models taking into account the structure of individual clouds as a way to explain the observations of galaxies on a kpc scale, so that information gained from studies of local star forming clumps can be used to understand star formation in galaxies too far away to compile detailed observations. Ultimately, these studies may help to constrain a universal star formation law.

In this paper, we present mapping observations of HCN (1–0), HCO^+ (1–0), HNC (1–0) and CS (2–1) towards ten high-mass clumps associated with H_2O masers in the Galaxy. Based on these data, and in combination with other previous studies, we can study the kinematics of GMCs, and investigate how the properties of dense gas tracers, such as their emissions, distributions, line profiles and ratios, as well as their chemistry, are affected by their ambient environments. We also present a preliminary analysis which allows us to investigate physical properties of star forming regions, as well as the difference between the molecules as dense gas tracers in detail. This paper is organized as follows: Section 2 describes the observations and data reduction. In Section 3, we present the spectra and velocity integrated intensity contour maps of these dense cores in four molecular lines, and discuss the spatial distributions of different tracers. We also use some diagnostics in various line ratios to compare our data with those of extragalactic observations in Section 3. A brief summary is given in Section 4.

2 OBSERVATIONS AND DATA REDUCTION

Our sample is a subset of the sample of dense clumps associated with H_2O masers, with several CS and HCN transitions surveyed (Plume et al. 1992, 1997; Mueller et al. 2002; Shirley et al. 2003; Wu et al. 2010). We select ten high-mass star forming cores with available Spitzer Multiband Imaging Photometer (MIPS) and Infrared Array Camera (IRAC) observations at the time of our observations. Their distances are less than 5 kpc, which allows us to detect the structure of the cores on a ∼1 pc scale, within which we think the real physical core is located. The sources are listed in Table 1.

Most observations were conducted during May 7 and 30 in 2005. We observed HCN (1–0), CS (2–1), HNC (1–0) and HCO^+ (1–0) with the 16-element focal plane array (SEQUOIA) on the Five College Radio Astronomy Observatory (FCRAO) 14 m telescope. The HCN (1–0) (88.631 GHz) and CS (2–1) (97.980 GHz) lines were observed with a dual channel correlator (DCC) simultaneously, and HNC (1–0) (90.663 GHz) and HCO^+ (1–0) (89.188 GHz) were obtained in the same way. The HCN (1–0) and CS (2–1) data of W3(OH), W44, W75N, W75(OH), S106, S87 and CEP A are collected from the PhD thesis of Wu (2006), which were also observed with the same facility in 2004 and 2005. The $T_{\rm sys}$ was about 180 K in Wu (2006), and about 250 K in our observations. All observations were performed with On-the-Fly mode, and were regridded to a sampling interval of 25″.

The full width at half maximum (FWHM) of the main beam of FCRAO was about 60″ at about 88.6 GHz. A velocity resolution of ∼0.1 km s^{-1} was achieved with the 25 MHz bandwidth on the DCC, which corresponds to a frequency resolution of ∼ 29.5 kHz. Each map covers an area of $\sim 10' \times 10'$, except for W75N, whose map covers an area of $\sim 15' \times 15'$.

Most of the emission lines have been confined in the mapped regions. The typical pointing error was $5'' - 10''$ (1σ, rms). All molecular line data were reduced with the GILDAS package[1]. Linear baselines were subtracted from the spectra. The antenna temperature ($T_{\rm A}^*$) was converted to main beam temperature ($T_{\rm mb}$) via $T_{\rm mb} = T_{\rm A}^*/\eta_{\rm FSS}\eta_c$, with $\eta_{\rm FSS} = 0.7$. The value of η_c depends on the source size, and for a typical map in this study ($\sim 10^{'}$), η_c = 0.7.

3 RESULTS AND DISCUSSION

3.1 Dense Gas Maps in Star Forming Cores

The velocity integrated intensity of each molecular line spectrum was computed in every sampled point. We derive the velocity integrated line intensity (I) in each pixel of the maps, with uniform velocity range for all the pixels in each molecular line and every source.

In Figure 1, we present the velocity integrated intensity contour maps of the four dense gas tracers for all targets. Data with signal to noise ratio $> 3\sigma$ are presented. In W3(OH), CEP A and S87, CS (2–1) and HCN (1–0) maps only have one single peak, and we show the contours starting from 2σ. In the following analysis, only those sampled points (25″ in diameter) with velocity integrated intensity $> 3\sigma$ are included. As shown in Figure 1, HCN (1–0), CS (2–1), HCO^+ (1–0) and HNC (1–0) generally trace a similar area in these massive dense cores, with comparable sizes and similar shapes. Most cores are resolved in our observations.

In BFS 11-B we identify three dense cores, and they are aligned from north to south. Among the three cores, the northern and the southern ones have similar intensities for all the four dense gas tracers, while the one in the middle varies a lot for different tracers. The HCO^+ (1–0) and HCN (1–0) emissions show similar intensity in the middle core. In the CS (2–1) contour map, the peak position of the middle core shifts towards the southern core, while in

[1] *http://www.iram.fr/IRAMFR/GILDAS/*

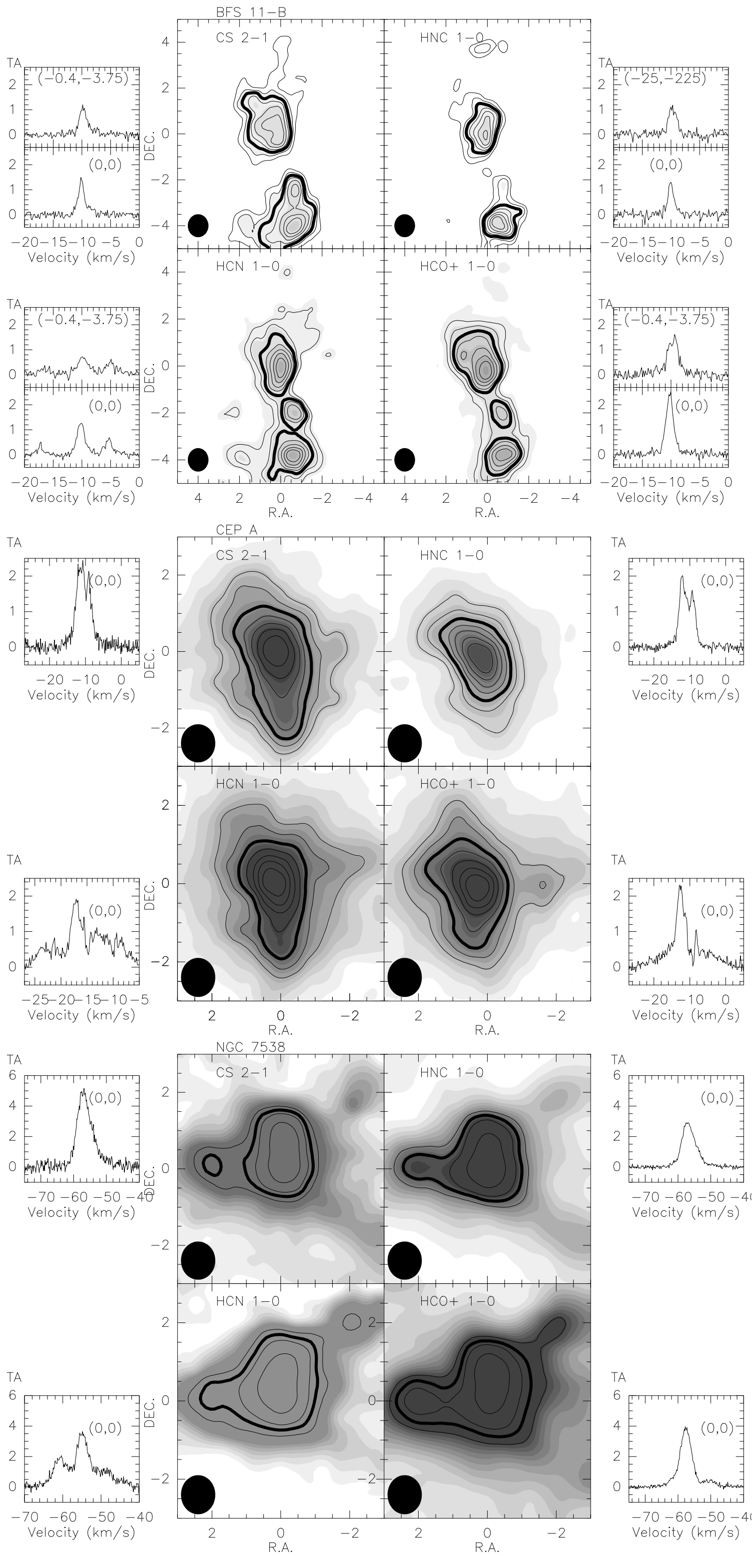

Fig. 1 Contours of the molecular integrated intensity observed toward each source with some example spectra. Beam sizes are indicated in the lower left corner of each panel. Contours are in steps of 10 percent of the peak intensity in BFS 11-b and Cep A, and 20 percent of the peak intensity in NGC 7538, S106, S255, S87, W3(OH), W44, W75N and W75(OH). The lowest contour is 30 percent of the peak intensity in BFS 11-b and Cep A, and 40 percent of the peak intensity in NGC 7538, S106, S255, S87, W3(OH), W44, W75N and W75(OH). The top part of each panel that shows a spectrum gives the coordinate where the spectrum was selected.

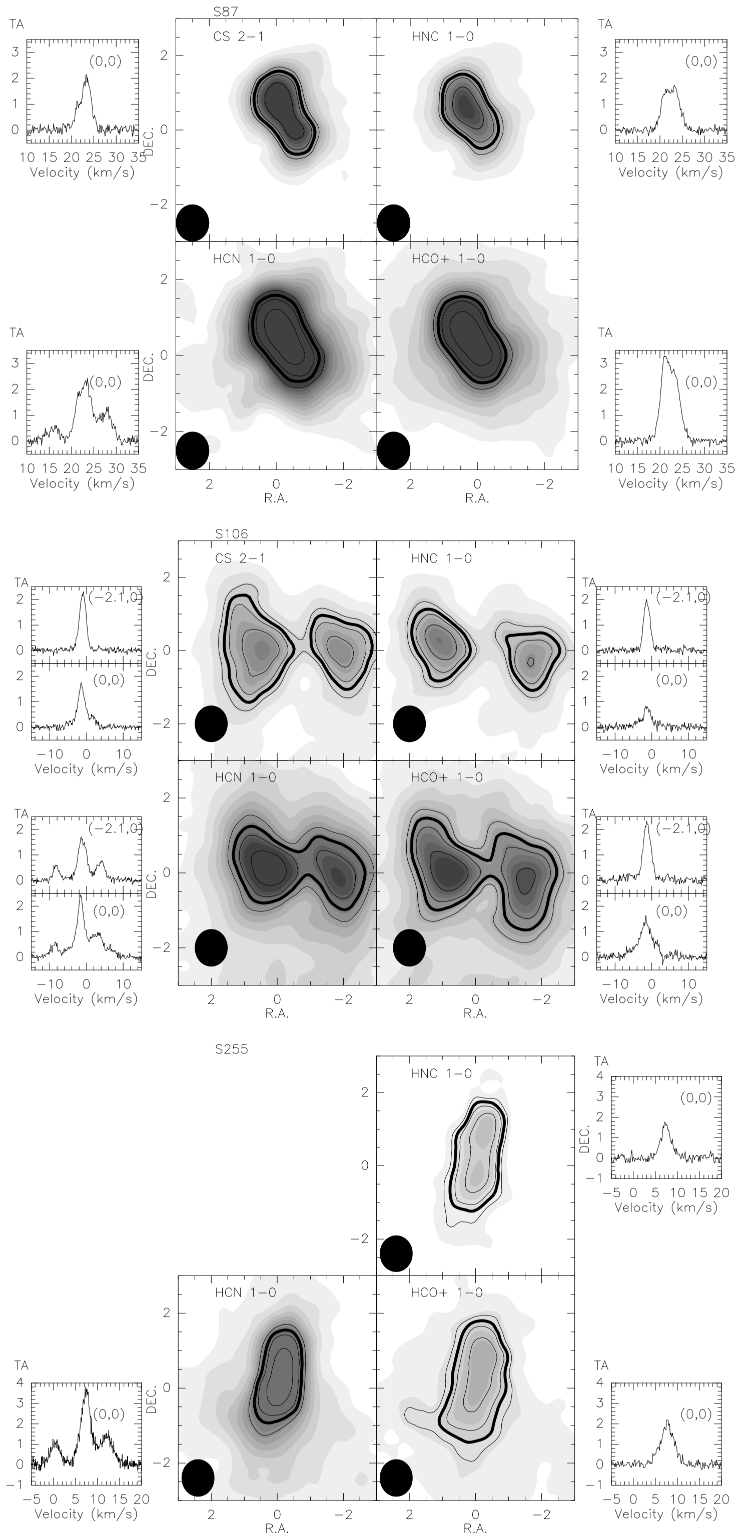

Fig. 1 — *Continued.*

the HNC (1–0) contour map, the middle one is almost invisible. This may reflect different excitation conditions or chemical environments for different cores within a single GMC.

We identify two cores each in W75(OH), S106, W44 and W75N. In NGC 7538, the distribution of all tracers displays an elongated structure, which shows a weaker compact component in the east, and an extended stronger

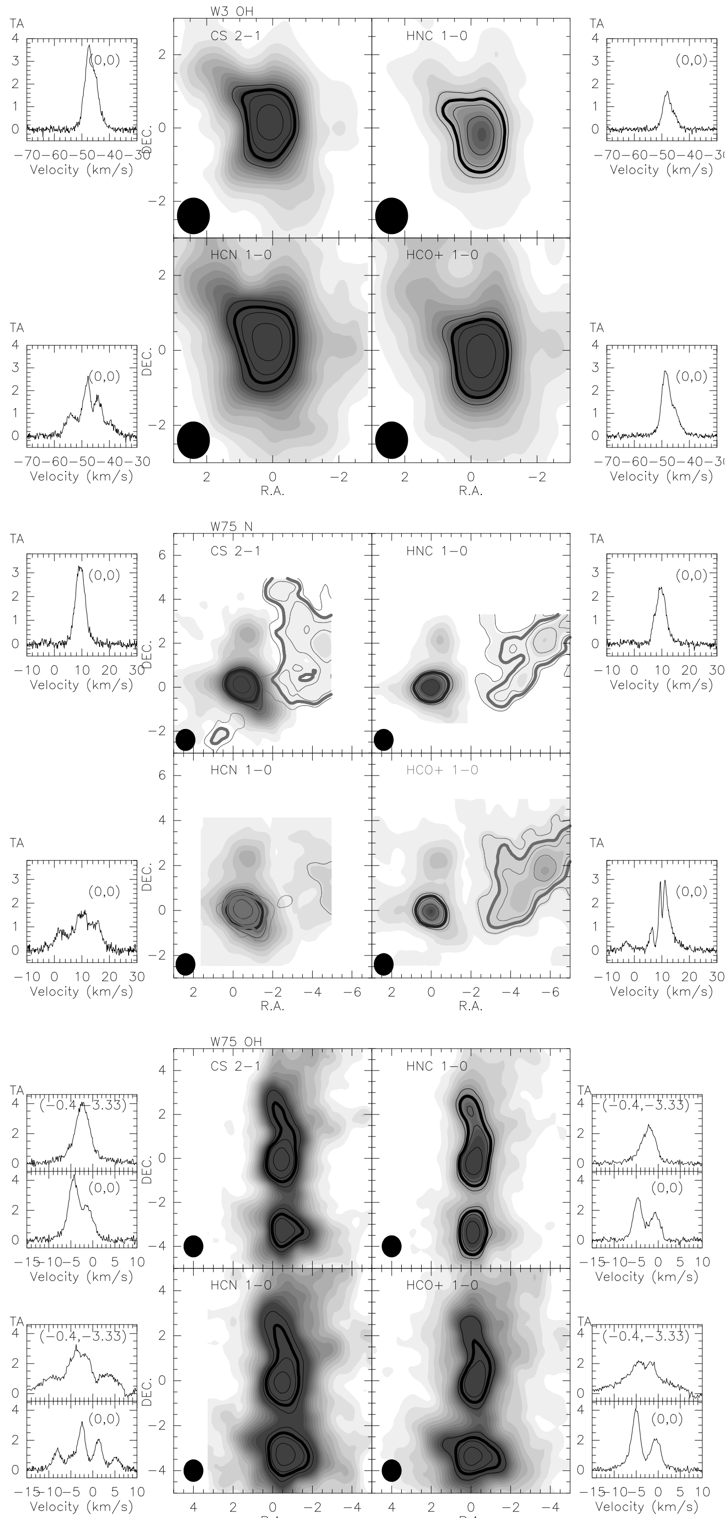

Fig. 1 — *Continued.*

emission component in the west. In W75N, we find that the two components have a large difference in velocity (13 km s^{-1}). We attribute this to be associated with different clouds along the same line of sight. One is compact and the other is extended. The similar distributions of different tracers for each source suggest that the excitation mechanism(s) may be similar for these four lines.

Six out of ten sources, W3(OH), W44, W75N, W75(OH), CepA and NGC 7538 - IRS9, have been observed by Reiter et al. (2011a) with 12 transitions from

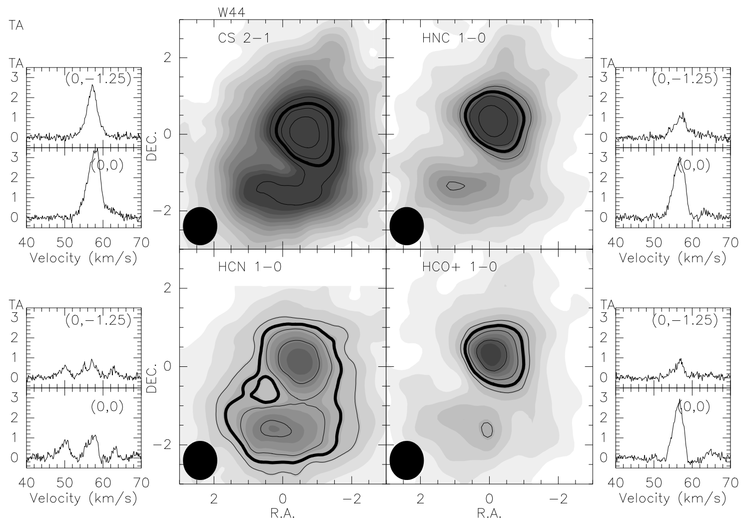

Fig. 1 — *Continued.*

Table 1 Mapping Surveys Toward Massive Clumps

Sources	RA. J2000	Dec. J2000	Distance (kpc)	Ref	Map size arcsec × arcsec
BFS 11-B	21:43:06.68	66:07:04.06	2.0	1	750 × 600
CEP A	22:56:18.14	62:01:46.31	0.73	2	400 × 450
S87	19:46:20.45	24:35:34.37	1.9	3	600 × 600
S106	20:27:25.74	37:22:51.81	4.1	4	600 × 600
W3(OH)	02:27:04.69	61:52:25.50	2.4	5	400 × 525
NGC 7538	23:13:44.85	61:26:50.67	2.8	6	600 × 575
W44	18:53:18.5	01:14:56.62	3.7	7	400 × 325
W75N	20:38:36.93	42:37:37.5	3.0	8	400 × 300
W75(OH)	20:39:01.01	42:22:49.84	3.0	8	550 × 800
S255	06:12:53.71	17:59:22.05	1.3	6	600 × 500

Notes: Map size indicates the area from which we extract the source-averaged spectra.

nine molecules, N_2H^+, $H^{13}CO^+$, HCS^+, CCH, HNC, $C^{34}S$ (5–4), SO, SO_2, and CH_3OH and some isotopologues. The transitions studied in their work represent diverse probes of the chemical and physical structures in these clumps. Most transitions trace a single emission peak centered near the dust continuum peak position. In W3(OH), W44, W75(OH) and CepA, the spatial difference between the N_2H^+ emission peak and that of HCO^+ supports these sources being chemically different. W3(OH), S255, W44, S87, S106, W75N, W75(OH), BFS 11-B, CepA and NGC 7538-IRS9 have also been mapped with CS (2–1), CS (7–6), HCN (1–0) and HCN (3–2) in Wu et al. (2010). Combining with the CS (5–4) map (Shirley et al. 2003), they can be utilized in a systematic analysis of massive, dense clumps by identifying tracers with a wide range of excitation conditions.

3.2 Spectral Analysis

In Figure 1, we plot four spectra beside each contour map. These are spectra from HCN (1–0), HNC (1–0), HCO^+ (1–0) and CS (2–1), which are extracted from the center position (0,0) of each core. All spectra are smoothed to a velocity resolution of 0.4 km s^{-1}. We see some wing features in some of the lines, which are asymmetric and/or significantly deviate from a Gaussian line profile. The spectra that show such features are CS (2–1) of BFS 11-B, CS (2–1) and HCO^+ of Cep A, HNC (1–0) and CS (2–1) of NGC 7538, CS (2–1), HNC (1–0) and HCO^+ of S106, and CS (2–1) of W44. This wing feature may be caused by outflow motion which has already been identified in Cep A (Bally & Lane 1991), NGC 7538 (Wu et al. 2004), S106 (Schneider et al. 2002), and W44 (Paron et al. 2009). Comparing our results with Wu et al. (2010), the $T_{\rm mb}$ and the velocity integrated intensity are consistent in most sources.

Molecular HCN transitions are often used as dense gas tracers. Its ground rotational transition, $J = 1 - 0$, has been surveyed in a large sample of Galactic high mass star forming cores (e.g., Wu et al. 2005). The critical densities ($n_{\rm crit}$) for all transitions in this paper at 10 K and 100 K are adopted from Evans (1999) and shown in Table 2. HCN (1–0) has hyperfine structure and its three transitions are separated by 2.1 MHz ($F = 1 - 0$ to $F = 2 - 1$) and 1.4 MHz ($F = 1 - 1$ to $F = 2 - 1$). The middle transition ($F = 2 - 1$) is optically thick, but the other two transitions are optically thin in these dense cores. We calculate the velocity integrated line intensity of the central HCN spectrum at position (0,0) with all three hyperfine lines in Table 3.

In Table 4 we present the peak temperature of the line ($T_{\rm mb}$), integrated intensity ($\int T_{\rm mb}{\rm d}\nu$), local standard of rest (LSR) velocity, and FWHM of CS (2-1), HNC (1–0) and HCO^+ (1–0) for the central map at position (0,0) in massive dense clumps. The $\int T_{\rm mb}{\rm d}\nu$ of the three lines towards the position (0, 0) for HCO^+ (1–0), HNC (1–0) and CS (2–1) in W75(OH) includes two peaks, and the mean $\int T_{\rm mb}{\rm d}\nu$ is 22.82, 16.57 and 25.67 K km s^{-1}, respectively. However, there are four emission peaks of HCN (1–0) identified at (0, 0). The FWHM of the line in (0, 0) is the same as that in $(-0.4, -3.33)$ for the same line, which indicates that the two or four peaks are present because of self-absorption. The double peaks with the blue profile reflect the higher inflow motion, which is consistent with the result in Wu et al. (2010). In order to get a rough idea of how strong the line emission is within the entire core regions, we average the spectra of all sampled points using the time weighting function[2], and show the averaged spectra in Figure 2.

According to Figure 2, the strongest emission among most sources is HCN (1–0), except in the three sources BFS11-b, S106 and W44. The second strongest emission is HCO^+ except in W44 and W75(OH). HNC is the weakest in all the sources except for W44. The typical abundance of HCO^+ is 5×10^{-10} in a diffuse cloud and 8×10^{-9} in a molecular cloud (Tielens 2013); for HCN it is 3×10^{-9} in a diffuse cloud and 2×10^{-8} in a molecular cloud; for HNC it is 6×10^{-10} in a diffuse cloud and 2×10^{-8} in a molecular cloud; for CS it is 3×10^{-9} in a diffuse cloud. However, the abundance of HCN in a dense core is not available. Although the abundance of the tracers will be one of the factors affecting the intensity of line emission, there are many other important factors. However, these molecular emissions are optically thick.

HCO^+ is known to be a good tracer of dense gas, especially for embedded molecular outflows (e. g., Codella et al. 2001; Hofner et al. 2001). It is an abundant molecule, with particularly enhanced abundances around regions of higher fractional ionization. It is also enhanced by outflows where shock-generated radiation fields are present (Rawlings et al. 2000, 2004). CS is also a very good tracer of dense gas, but in cold dark clouds the CS emission vanishes toward the center of the core because of depletion (Vasyunina et al. 2011). Infrared (IR) pumping might indeed play a vital role in the case of HCN emission and the abundance ratio HCN/HNC strongly depends on temperature (Vasyunina et al. 2011).

In some targets, as shown in Figure 1, the line profiles of these tracers appear to be asymmetric, and the asymmetry varies from line to line. HCO^+ normally shows the clearest signature of deviation from a Gaussian profile, while CS lines are close to a Gaussian profile. Most of these targets show blue-asymmetries which indicate the presence of infall. However, W75N and CEP A show contradictory line profiles in different tracers. Their HNC lines have blue asymmetry and HCO^+ lines have red asymmetry (Reiter et al. 2011b). However in our low-J HCO^+ and CS spectra, there is no indication of asymmetry, although their $J=3-2$ lines do show asymmetry in Reiter et al. (2011b). This tells us that low J line profiles alone cannot conclusively identify the dynamics of massive cores. There is no totally reliable indicator for infall or outflow, so models and more information are needed for a better diagnostic. On the other hand, these massive dense cores have very high average volume density (e.g., Plume et al. 1997; Mueller et al. 2002), so tracers with higher critical density (higher J transitions, or HCN better than HNC/CS) are better for exploring the infall signature.

[2] Spectra were averaged with software which can be downloaded from *http://www.iram.fr/IRAMFR/GILDAS/*, by sequentially adding channels using the weighting function Time * abs (Fres) / (Tsys^2).

3.3 Comparison of Line Ratios

3.3.1 The results from comparing line ratios

Table 5 presents the averaged velocity integrated intensity of spectra covering all the sampled points, and the averaged spectrum is shown in Figure 2. The integrated intensity ratios are also given in the table. Hereafter, we use $I_{\rm HCN}$ to represent the velocity integrated intensity of HCN (1–0), $I_{\rm HCO+}$ that for HCO^+ (1–0), $I_{\rm CS}$ that for CS (2–1) and $I_{\rm HNC}$ that for HNC (1–0). We use $I_{\rm HCN}/I_{\rm HCO+}$ to represent the velocity integrated intensity ratio of HCN (1–0) to HCO^+ (1–0).

We compare line ratios for six GMC cores as shown in Figure 3. To discern collective behavior of the high density tracer molecules HCN, HCO^+, CS and HNC within the real molecular cores, we only include lines within the range of 1 pc of the peak emission (we assume that the physical radius of the real inner core is 1 pc). The numbers of sampled points vary among the six GMC cores, because the distances of the six GMCs are different, i.e. within circles with the same physical radius, the farther away the GMC is from us, the less sampled points are included in the circle, as demonstrated in Figure 3. Velocity integrated intensity ratios of dense gas tracers are associated with the properties of their surrounding environments. In the top left panel of Figure 3, all the points tend to be distributed from top left to bottom right. In the top right panel, all the points tend to be distributed from top right to bottom left. In all three panels, most points are clustered except for the points from W44, represented by green triangles. Here and in the rest of the paper, we use $\log {\rm HCO^+}/\log {\rm HCN}$ for $\log I_{\rm HCO+}/\log I_{\rm HCN}$, and $\log {\rm HNC}/\log {\rm HCO^+}$ for $\log I_{\rm HNC}/\log I_{\rm HCO+}$.

3.3.2 Interpretations with known processes in galaxies

The velocity integrated line intensity ratio of characteristic tracer molecules may be interpreted using the contributions of two distinct components: PDRs and outflow-related me-

Table 2 Properties of Density Probes

Molecule	Transition	ν (GHz)	n_c (10 K) (cm^{-3})	n_c (100 K) (cm^{-3})
HCN	$J = 1 - 0$	88.631	2.6×10^6	4.5×10^6
HCO$^+$	$J = 1 - 0$	89.188	1.7×10^5	1.9×10^5
HNC	$J = 1 - 0$	90.663	2.8×10^5	4.0×10^5
CS	$J = 2 - 1$	97.980	3.0×10^5	3.9×10^5

Notes: The last two columns are adopted from Evans (1999).

Table 3 Observational Results of HCN Transitions

Sources	HCN $T_{\rm mb(k)}$ (K) ($F = 1 - 0$) (K)	$T_{\rm mb(k)}$ ($F = 2 - 1$) (K)	$T_{\rm mb(k)}$ ($F = 1 - 1$) (K)	$\int T_{\rm mb} d\nu$ (all hpf Fs) (K km s^{-1})	$V_{\rm LSR}$ ($F = 2 - 1$) (km s^{-1})	FWHM ($F = 2 - 1$) (km s^{-1})
BFS 11-B	0.7 (0.08)	2.6 (0.08)	1.2 (0.08)	7.7 (0.08)	–10.17 (0.02)	1.69 (0.06)
CEP A	1.1 (0.14)	2.9 (0.14)	1.7 (0.14)	28.6 (0.10)	–17.17 (0.03)	2.01 (0.08)
S87	1.0 (0.13)	4.6 (0.13)	2.2 (0.13)	30.0 (0.11)	22.89 (0.03)	3.93 (0.09)
S106	0.9 (0.18)	4.3 (0.18)	1.7 (0.18)	25.8 (0.07)(d)	–1.59 (0.17)	3.48 (0.17)
W3(OH)	1.9 (0.10)	...	...	43.3 (0.08)	...	...
NGC 7538	3.7 (0.18)	6.3 (0.18)	2.0 (0.18)	66.8 (0.16)	–57.47 (0.04)	3.81 (0.13)
W44	1.7 (0.16)	2.2 (0.16)	1.1 (0.16)	14.1 (0.10)	57.21 (0.05)	2.93 (0.11)
W75N	1.6 (0.13)	3.1 (0.13)	2.2 (0.13)	40.0 (0.10)	9.84 (0.09)	4.98 (0.15)
W75(OH)	...	...	...	45.3 (0.11)	...	...
S255	2.1 (0.18)	7.0 (0.18)	2.8 (0.18)	37.6 (0.16)	7.36 (0.02)	2.74 (0.05)

Table 4 Observational Results of HCO$^+$, HNC and CS Transitions

Sources	HCO$^+$ $T_{\rm mb(k)}$ (K)	$\int T_{\rm mb} d\nu$ (K km s^{-1})	$V_{\rm LSR}$ (km s^{-1})	FWHM (km s^{-1})	HNC $T_{\rm mb(k)}$ (K)	$\int T_{\rm mb} d\nu$ (K km s^{-1})	$V_{\rm LSR}$ (km s^{-1})	FWHM (km s^{-1})	CS $T_{\rm mb(k)}$ (K)	$\int T_{\rm mb} d\nu$ (K km s^{-1})	$V_{\rm LSR}$ (km s^{-1})	FWHM (km s^{-1})
BFS 11-B	4.80 (0.10)	8.30 (0.09)	–10.21(0.02)	1.62 (0.04)	2.51 (0.13)	3.46 (0.09)	–10.01(0.03)	1.30 (0.08)	2.63 (0.14)	3.95 (0.07)	–10.08 (0.02)	1.41 (0.07)
CEP A	3.92 (0.33)	17.20 (0.33)	–12.56 (0.06)	4.12 (0.26)	3.45 (0.25)	17.29 (0.09)	–11.04 (0.02)	4.71 (0.05)	4.49 (0.24)	22.02 (0.15)	–10.66 (0.03)	4.60 (0.07)
S87	6.67 (0.25)	30.31 (0.11)	22.13 (0.02)	4.26 (0.03)	3.51 (0.15)	15.64 (0.10)	22.46 (0.028)	4.19 (0.06)	3.82 (0.19)	12.7 (0.12)	23.14 (0.03)	3.13 (0.07)
S106	2.55 (0.15)	12.85 (0.12)	–1.58 (0.04)	4.75 (0.11)	1.40 (0.16)	4.72 (0.11)	–1.31 (0.06)	3.17 (0.23)	3.02 (0.18)	9.39 (0.09)	–1.28 (0.02)	2.92 (0.08)
W3(OH)	2.86 (0.26)	28.71 (0.09)	–48.07 (0.02)	5.15 (0.04)	3.06 (0.13)	14.33 (0.08)	–47.83 (0.03)	4.39 (0.06)	7.0 (0.20)	37.63 (0.11)	–46.84 (0.01)	5.05 (0.03)
NGC 7538	7.59 (0.17)	35.49 (0.19)	–57.62 (0.02)	4.39 (0.06)	5.73 (0.15)	30.41 (0.11)	–56.79 (0.02)	4.99 (0.04)	9.63 (0.34)	54.37 (0.35)	–56.75 (0.03)	5.30 (0.08)
W44	5.71 (0.23)	17.28 (0.12)	56.39 (0.02)	2.84 (0.04)	5.88 (0.16)	22.29 (0.13)	56.59 (0.02)	3.54 (0.05)	5.29 (0.16)	21.94 (0.11)	57.65 (0.02)	3.9 (0.05)
W75N	4.80 (0.40)	26.63 (0.11)	10.90 (0.03)	5.21 (0.06)	4.71 (0.14)	22.53 (0.12)	9.64 (0.02)	4.48 (0.06)	6.73 (0.11)	29.86 (0.11)	9.41 (0.02)	4.16 (0.04)
W75(OH)	...	35.90 (0.10)	...	...	...	24.77 (0.09)	...	...	...	39.18 (0.12)	...	...
S255	3.92 (0.16)	15.41 (0.14)	7.70 (0.03)	3.70 (0.08)	3.27 (0.13)	9.54 (0.13)	7.38 (0.04)	2.75 (0.09)	...	...	...	...

chanical heating-dominated regions (Baan et al. 2014). In GMCs, once a star is formed, the stellar ultraviolet (UV) radiation creates a PDR (Hollenbach & Tielens 1999). In galaxies, the variations in the velocity integrated molecular line intensity ratios are related to the circumnuclear radiation field, in the sense that different power sources, such as an Active Galactic Nucleus (AGN) or starburst, excite the molecular lines (Kohno et al. 2001, Graciá-Carpio et al. 2006). Although there are many observational studies that have been done to analyze the molecular ISM in nearby galaxies (e.g. Gao & Solomon 2004b; Graciá-Carpio et al. 2006; Baan et al. 2008), an interpretation for the variety of phenomenology related to the Galactic ISM that can serve as a general benchmark using comparable extragalactic observations is still lacking (Baan et al. 2014). After a 65 galaxy (including 10 ultraluminous galaxies) HCN survey was completed, Gao (2007) showed a tight linear correlation between HCN and IR (star forming rate) extending to high redshift QSOs. Gao et al. (2007) found that the far-IR/HCN ratios in high-redshift sources lie systematically above the far-IR/HCN correlation established for nearby galaxies by about a factor of 2. By contrast, Wu et al. (2005) connected GMC dense cores to galaxies near and far, and found that the correlation continues to a much smaller scale, with nearly the same ratio of IR luminosity to HCN luminosity, after adding 47 Galactic star forming cores into this correlation. Here we cast this idea from galaxy study to Galactic star forming regions, using PDR and XDR features to study the radiation field of massive dense cores. The PDRs are dominated by far-UV photons generated by massive stars, while X-rays in massive star forming regions are usually related to shocks created by high-velocity stellar winds from massive stars. Comparing observations with PDR and XDR models will help us to better understand the environment in massive star forming regions in the Milky Way.

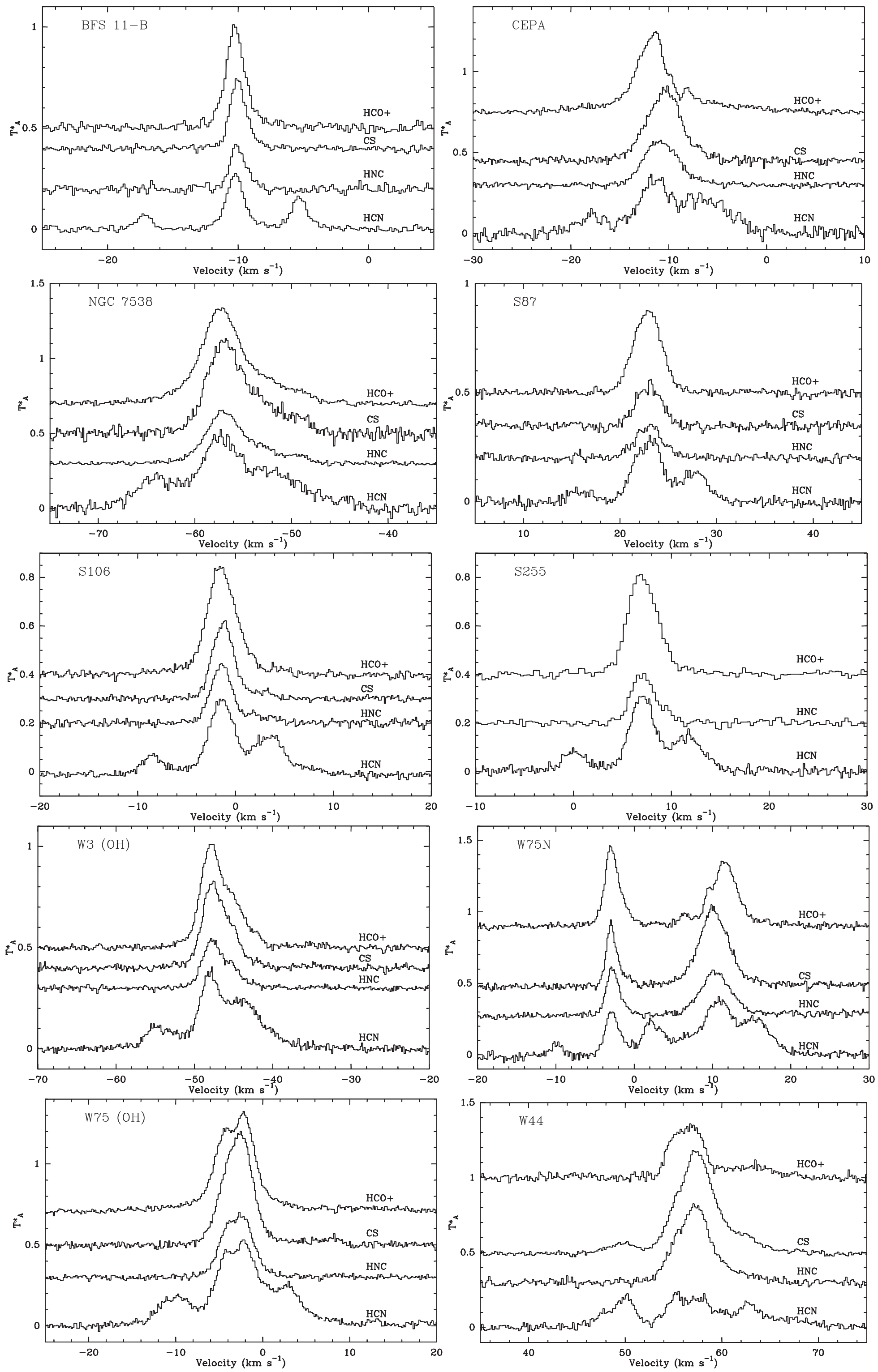

Fig. 2 Spectra of HCN (1–0), HNC (1–0), HCO^+ (1–0) and CS (2–1) averaged over all the sampled points from each source.

By observing IR luminosity sources with known OH megamaser activity, Baan et al. (2008) studies the $I_{\mathrm{HCO+(1-0)}}/I_{\mathrm{HCN(1-0)}}$ and $I_{\mathrm{HNC(1-0)}}/I_{\mathrm{HCN(1-0)}}$ ratios of galaxies as indicators of environments affected by star-formation feedback. In PDRs which are dominated by massive star formation and in XDRs which are generally powered by AGNs, the chemical structure and thermal balance are completely determined by the radiation field, such as UV photons or X-rays. Distinguishing whether observed features are generated by far-UV photons or by X-rays

Table 5 The Averaged Integrated Intensity of HCN, HCO^+, HNC and CS, and the Ratios Among Them

Sources	I_{HCN}	I_{HCO^+}	I_{HNC}	I_{CS}	$I_{HCN(F=2-1)}$	I_{HCN}/I_{HCO^+}	I_{HCN}/I_{HNC}	I_{HCN}/I_{CS}	I_{HCO^+}/I_{HNC}	I_{HCO^+}/I_{CS}	I_{HNC}/I_{CS}
			(K km s^{-1})								
BFS 11-B	1.863	2.198	0.653	1.184	0.518	0.847	2.853	1.574	3.365	1.856	0.551
CEP A	5.980	5.027	2.471	4.024	1.322	1.189	2.419	1.485	2.033	1.248	0.614
S87	3.261	2.824	1.063	1.055	0.935	1.154	3.067	3.090	2.656	2.676	1.007
S106	3.282	3.670	1.588	1.953	0.928	0.894	2.066	1.680	2.311	1.878	0.812
W3(OH)	6.318	5.161	2.094	3.847	1.381	1.224	3.017	1.642	2.464	1.341	0.544
NGC 7538	10.343	8.443	4.218	7.716	2.585	1.225	2.451	1.340	2.001	1.094	0.546
W44	5.357	3.831	5.127	7.465	1.202	1.398	1.044	0.717	0.747	0.513	0.686
W75N	9.535	7.294	3.031	5.853		1.307	3.146	1.629	2.406	1.246	0.517
W75(OH)	9.710	7.382	3.582	6.359	2.684	1.315	2.711	1.526	2.060	1.160	0.563
S255	3.794	3.363	1.3	...	0.999	1.128	2.918	...	2.587	...	...

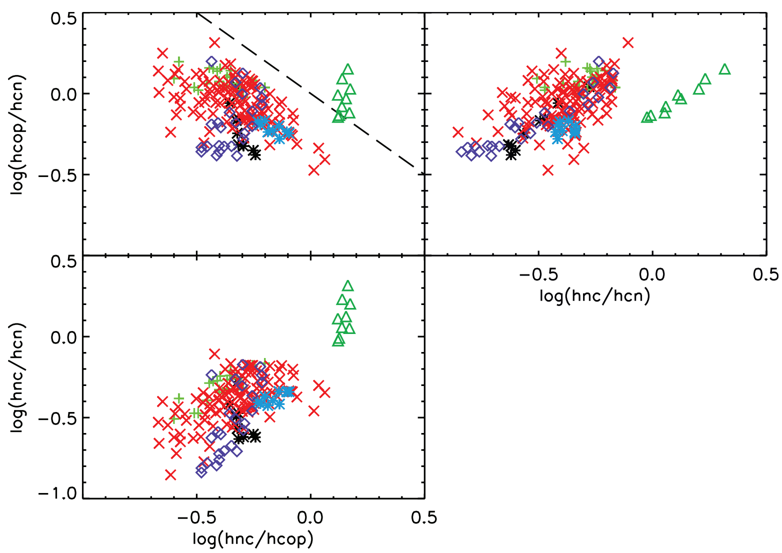

Fig. 3 The velocity integrated line ratios of HCN (1–0), HNC (1–0) and HCO^+ (1–0) versus each other. *Top-left*: integrated $I_{HCO^+(1-0)}/I_{HCN(1-0)}$ versus $I_{HNC(1-0)}/I_{HCO^+(1-0)}$ ratios; *top-right*: integrated $I_{HCO^+(1-0)}/I_{HCN(1-0)}$ versus $I_{HNC(1-0)}/I_{HCO^+(1-0)}$ ratios; and *bottom-left*: integrated $I_{HNC(1-0)}/I_{HCN(1-0)}$ versus $I_{HNC(1-0)}/I_{HCO^+(1-0)}$ ratios. The dashed line separates the regions representing the line ratio of predominantly photodominated regions (PDRs) from predominantly X-ray dominated regions (XDRs). The green triangle symbols are for W44, the purple rhombus symbols are for S87 , the green plus symbols are for BFS 11-b, the black asterisk symbols are for W3(OH), the red cross symbols are for Cep A, and the blue asterisk symbols are for NGC 7538.

has become increasingly important as a diagnostic tool for astrophysical environments with the advent of IR and (sub-) millimeter telescopes (Meijerink & Spaans 2005). Differences in the spatial distribution of the emission of HCN and HNC directly reflect the variations in chemical abundance. The I_{HNC}/I_{HCN} ratio is 0.318 $\sim$ 0.958 in our sample, which is similar to that of IC 342, but smaller than the value 3.0 (Churchwell et al. 1984) found in dark clouds, and greater than that 0.2 (Schilke et al. 1992) in the Orion hot core. The range of the I_{HCN}/I_{HCO^+} ratio is $0.9 \sim 1.4$, which is higher than in AGN galaxies but lower than in starburst galaxy M82, as shown in Figure 3.

We use this model as a benchmark for interpreting Galactic star formation regions. All sources except W44 have been observed with Chandra. After checking the archive data reduced by the pipeline, we find that there are a few X-ray emissions in S87, BFS 11-b, CEP A, W3(OH), NGC 7538, W75N, W75(OH) and S106, and there is a stronger X-ray point emission in S255. However, the data from source W44 are still unavailable until now. The points in most cloudy cores are congregated no matter if there are X-ray emissions. However, according to the literature, W44 is a supernova remnant which has been studied in many works. There is a very extended shell of X-ray emission around the molecular cloudy core (e.g. Jones et al. 1993; Seta et al. 2004), implying W44 could be more affected by shock excited X-rays than other sources. According to the diagnosis tool of XDRs and PDRs used in the OH megamaser sources, I_{HCO^+}/I_{HCN} vs. I_{HNC}/I_{HCO^+}, we conclude that the environment in the central region of W44 is similar to that in XDR regions. This agrees with the picture that most of the massive dense cores in our sample are dominated by UV photons from bright O or B stars, in spite of the weak X-ray emission from point sources, except W44, in which X-ray emission dominates. Also, X-rays can penetrate further than far-UV, so they could be more efficient for heating processes (Lahuis et al. 2007).

However, the influence of X-ray emissions on molecular chemistry is not yet clear in the complicated dynamics of GMCs, and there are a few other processes that need to be considered. There is an unusually high $I_{\rm HCN}/I_{\rm CO}$ ratio in the circumnuclear disk of Seyfert galaxy NGC 1068 (Tacconi et al. 1994). Meijerink & Spaans (2005) construct a model in which the abundance of $\rm HCO^+$ increases with an increasing ionization rate until some point, and decreases afterwards. The model $\rm HCNH^+ + e^- \rightarrow HCN/HNC + H$, which either slightly favors HNC over HCN (Shiba et al. 1998) or they are equally probable (Talbi & Herbst 1998), can be used in a highly ionized medium. Alternatively, the ratios for $I_{\rm HNC}/I_{\rm HCN}$ and $I_{\rm HCO^+}/I_{\rm HCN}$ are a function of total hydrogen column density as shown in the model. However, the abundance of $\rm HCO^+$ is effected by many processes, such as outflow and inflow (Reiter et al. 2011b). The $\rm HCO^+$ should depend on the density, but there is no significant discrepancy in the distribution between the data points from inside the GMC and those from outside the GMC. Higher resolution data and multi-line data are needed.

3.4 LAMOST Perspective

The large scale environments that have stellar populations surrounding these dense cores will potentially offer interesting opportunities for research using LAMOST. The large sky spectral survey conducted by LAMOST can provide important information on stellar components, such as metallicity, age, spatial distribution, kinematics, etc. This essentially reflects the final stage of stars on the main sequence that form within molecular clouds of interest (Zinnecker & Yorke 2007). By comparing the physical parameters of mature stars with those of star forming cores as well as young stellar objects, the interplay between the gas and stellar components in the proximity can be revealed. First of all, the evolutionary stages diagnosed by different molecular lines can be compared with the ages of the stars derived by near-IR photometry and those from LAMOST spectra. This will enable a multiwavelength investigation of the evolving behaviors of local star forming clouds. Second, the spatial and velocity information of these stars can also help to examine how the overall environment affects the survival of star clusters. In our future work, we will focus on star clusters and future LAMOST spectra of stars inside star clusters that are possibly associated with some dense cores or their local neighborhood by utilizing IR and radio/mm observations.

4 SUMMARY

We observed 10 massive star forming cores in the Galaxy, each with a fully sampled map over regions at least $10' \times 10'$ in area with HCN (1–0), $\rm HCO^+$ (1–0), HNC (1–0) and CS (2–1) lines. They were drawn from the sample selected from water maser surveys and found to have SPITZER IRAC and/or MIPS observations. We present the velocity integrated intensity contour maps of the four lines for all the sources. The distance between two points is $25''$, and the contour map was made from interpolation among the integrated intensity of the sampled points. We identify three dense cores in BFS 11-B, and two cores in W75(OH), S106, W44 and W75N.

In order to investigate the nature of emission in the whole core region, we average the spectra of all the sampled points. According to the velocity integrated intensity of the averaged spectra from the dense cores, the strongest emission among all sources is HCN (1–0), except in BFS11-b, S106 and W44. The second strongest emission is $\rm HCO^+$ except in W44 and W75(OH). The weakest emission comes from HNC except for W44.

We also try to interpret the radiation field of the star forming regions. We use the velocity integrated line intensity ratios as a diagnostic diagram of the radiation field according to the Baan et al. 2008 model that can be applied to galaxies. According to the diagnostic tool of XDR and PDR used in the OH megamaser sources, $I_{\rm HCO^+}/I_{\rm HCN}$ vs. $I_{\rm HNC}/I_{\rm HCO^+}$, we conclude that the environment in the central region of W44 is similar to that of XDR regions.

Acknowledgements We thank Mark Heyer and the staff of the FCRAO for their help during our observing runs. The authors would like to thank Professors Junzhi Wang, Xianzhong Zheng, Drs. Yinghe Zhao, Zhiyu Zhang and Xuejian Jiang, and Chentao Yang for useful discussions. This work is supported by the National Natural Science Foundation of China (Grant No. 11390373).

References

Baan, W. A., Henkel, C., Loenen, A. F., Baudry, A., & Wiklind, T. 2008, A&A, 477, 747
Baan, W. A., Loenen, A. F., & Spaans, M. 2014, MNRAS, 445, 3331
Bally, J., & Lane, A. P. 1991, ASIC, 342, 471
Beuther, H., & Steinacker, J. 2007, ApJ, 656, L85
Carpenter, J. M., Heyer, M. H., & Snell, R. L. 2000, ApJS, 130, 381
Cesaroni, R., Palagi, F., Felli, M., et al. 1988, A&AS, 76, 445
Churchwell, E., Nash, A. G., & Walmsley, C. M. 1984, ApJ, 287, 681
Codella, C., Bachiller, R., Nisini, B., Saraceno, P., & Testi, L. 2001, A&A, 376, 271
Elmegreen, B. G., & Clemens, C. 1985, ApJ, 294, 523
Evans, II, N. J. 1999, ARA&A, 37, 311
Gao, Y. 2007, in IAU Symposium, 237, eds. B. G. Elmegreen, & J. Palous, 331
Gao, Y., Carilli, C. L., Solomon, P. M., & Vanden Bout, P. A. 2007, ApJ, 660, L93
Gao, Y., & Solomon, P. M. 2004a, ApJ, 606, 271
Gao, Y., & Solomon, P. M. 2004b, ApJS, 152, 63
Garcia-Burillo, S., Usero, A., Fuente, A., et al. 2011, in IAU Symposium, 280, IAU Symposium, eds. J. Cernicharo, & R. Bachiller, 170P

Graciá-Carpio, J., García-Burillo, S., Planesas, P., & Colina, L. 2006, ApJ, 640, L135
Hofner, P., Wiesemeyer, H., & Henning, T. 2001, ApJ, 549, 425
Hollenbach, D. J., & Tielens, A. G. G. M. 1999, Reviews of Modern Physics, 71, 173
Jones, L. R., Smith, A., & Angelini, L. 1993, MNRAS, 265, 631
Kohno, K., Matsushita, S., Vila-Vilaró, B., et al. 2001, in Astronomical Society of the Pacific Conference Series, 249, The Central Kiloparsec of Starbursts and AGN: The La Palma Connection, eds. J. H. Knapen, J. E. Beckman, I. Shlosman, & T. J. Mahoney, 672
Lada, C. J., & Lada, E. A. 2003, ARA&A, 41, 57
Lahuis, F., van Dishoeck, E. F., Blake, G. A., et al. 2007, ApJ, 665, 492
Larson, R. B. 1994, in Lecture Notes in Physics, Berlin Springer Verlag, 439, The Structure and Content of Molecular Clouds, eds. T. L. Wilson, & K. J. Johnston, 13
Leroy, A. K., Lee, C., Schruba, A., et al. 2013, ApJ, 769, 12
Li, J., Wang, J., Gu, Q., Zhang, Z.-y., & Zheng, X. 2012, ApJ, 745, 47
Meijerink, R., & Spaans, M. 2005, A&A, 436, 397
Mueller, K. E., Shirley, Y. L., Evans, II, N. J., & Jacobson, H. R. 2002, in Astronomical Society of the Pacific Conference Series, 267, Hot Star Workshop III: The Earliest Phases of Massive Star Birth, ed. P. Crowther, 395
Paron, S., Ortega, M. E., Rubio, M., & Dubner, G. 2009, A&A, 498, 445
Plume, R., Jaffe, D. T., & Evans, II, N. J. 1992, ApJS, 78, 505
Plume, R., Jaffe, D. T., Evans, II, N. J., Martín-Pintado, J., & Gómez-González, J. 1997, ApJ, 476, 730
Rawlings, J. M. C., Taylor, S. D., & Williams, D. A. 2000, MNRAS, 313, 461
Rawlings, J. M. C., Redman, M. P., Keto, E., & Williams, D. A. 2004, MNRAS, 351, 1054
Reiter, M., Shirley, Y. L., Wu, J., et al. 2011a, ApJS, 195, 1
Reiter, M., Shirley, Y. L., Wu, J., et al. 2011b, ApJ, 740, 40
Schilke, P., Walmsley, C. M., Pineau Des Forets, G., et al. 1992, A&A, 256, 595
Schneider, N., Simon, R., Kramer, C., Stutzki, J., & Bontemps, S. 2002, A&A, 384, 225
Seta, M., Hasegawa, T., Sakamoto, S., et al. 2004, AJ, 127, 1098
Shiba, Y., Hirano, T., Nagashima, U., & Ishii, K. 1998, J. Chem. Phys., 108, 698
Shirley, Y. L., Evans, II, N. J., Young, K. E., Knez, C., & Jaffe, D. T. 2003, ApJS, 149, 375
Tacconi, L. J., Genzel, R., Blietz, M., et al. 1994, ApJ, 426, L77
Talbi, D., & Herbst, E. 1998, A&A, 333, 1007
Tielens, A. G. G. M. 2013, Reviews of Modern Physics, 85, 1021
Vasyunina, T., Linz, H., Henning, T., et al. 2011, A&A, 527, A88
Wu, Y., Wei, Y., Zhao, M., et al. 2004, A&A, 426, 503
Wu, J., Evans, II, N. J., Gao, Y., et al. 2005, ApJ, 635, L173
Wu, J. 2006, Massive Star Formation, from the Milky Way to Distant Galaxies, PhD Thesis, The University of Texas at Austin
Wu, J., Evans, II, N. J., Shirley, Y. L., & Knez, C. 2010, ApJS, 188, 313
Zhang, Z.-Y., Henkel, C., Gao, Y., et al. 2014, A&A, 568, A122
Zinnecker, H., & Yorke, H. W. 2007, ARA&A, 45, 481